nature portfolio

https://doi.org/10.1038/s41561-021-00853-7

Supplementary information

Marsh resilience to sea-level rise reduced by storm-surge barriers in the Venice Lagoon

In the format provided by the authors and unedited

Supplementary Information for

“Marsh resilience to sea-level rise reduced by storm-surge barriers in the Venice Lagoon”

Davide Tognin[1,2*], Andrea D’Alpaos[2,3], Marco Marani[1,2] and Luca Carniello[1,2]

[1] Department of Civil, Environmental, and Architectural Engineering, University of Padova, Padova, Italy.

[2] Center for Lagoon Hydrodynamics and Morphodynamics, University of Padova, Padova, Italy

[3] Department of Geosciences, University of Padova, Padova, Italy

*e-mail: davide.tognin@phd.unipd.it

Vertical accretion rate. The vertical accretion rate in each station is measured yearly through coring and measuring the layer deposited over the kaolinite horizon marker. Comparison between measured and computed accretion rate (Supplementary Figure 1) confirms that the adopted sediment traps offer a reliable measure of sedimentation.

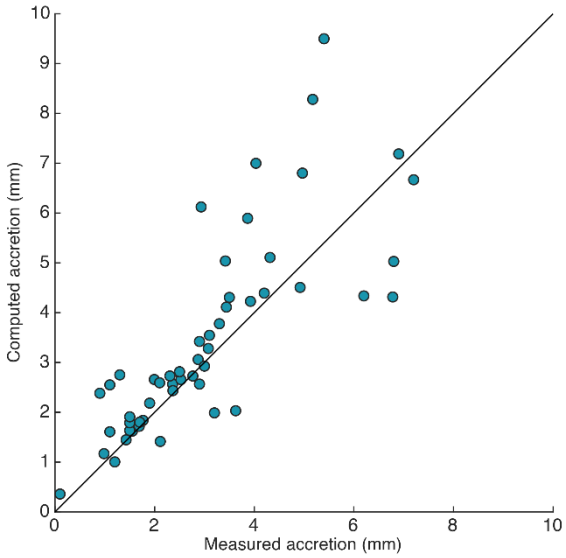

Supplementary Figure 1. Measured vs. computed vertical accretion. Scatter plot of yearly vertical accretion measured with horizon marker and accretion computed with sediment accumulation data and bulk density.

Storm-dominated period classification.

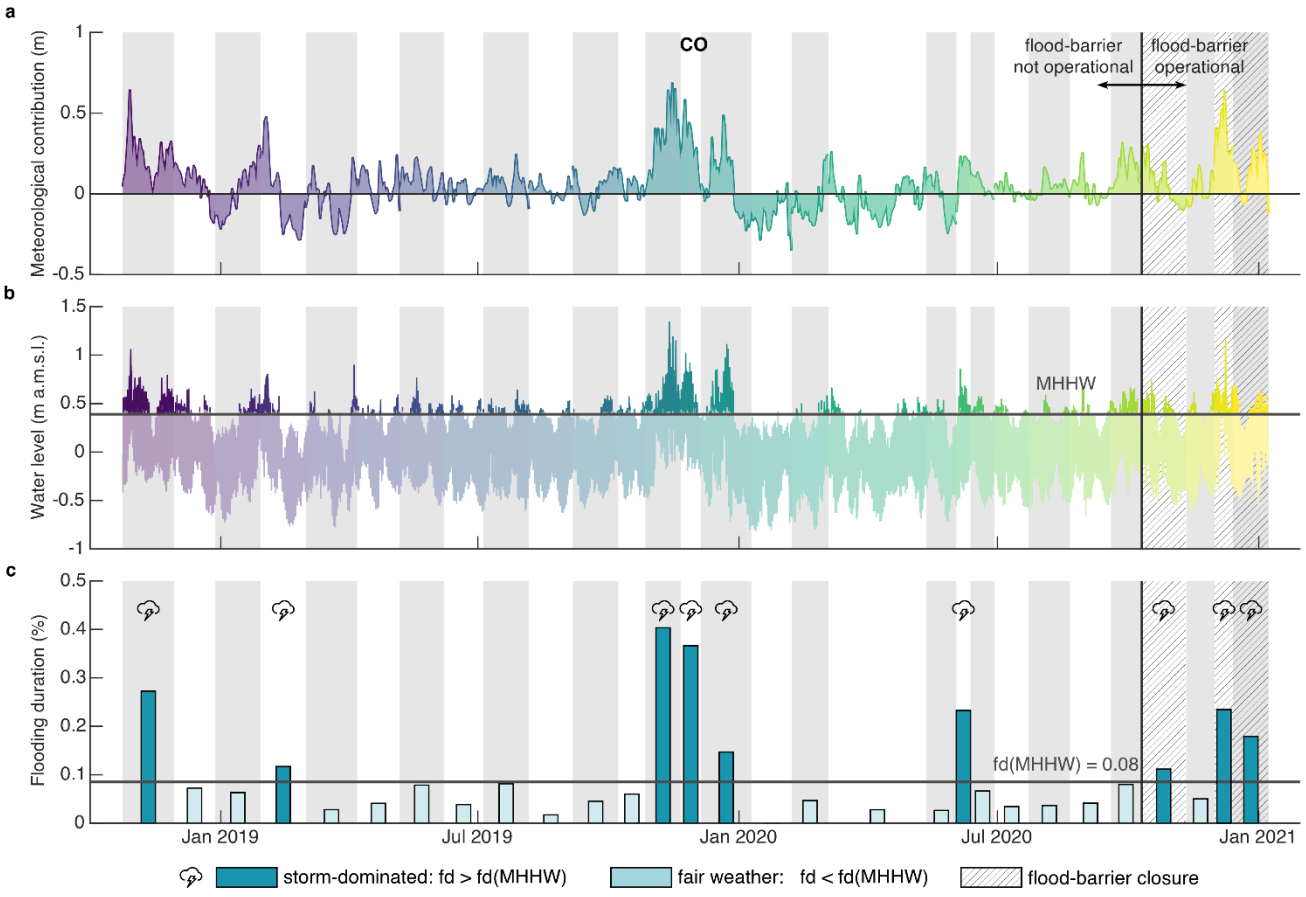

Supplementary Figure 2. Storm-dominated period classification (example for CO study area). (**a**) meteorological contribution to the tide; (**b**) measured water level and MHHW (dark gray line); (**c**) comparison between the flooding duration of MHHW (fd(MHHW) = 0.08, dark gray line) and the flooding duration (fd) of each period. Alternate white and grey background indicates different observation periods, hatched background indicates periods with real closures of flood barriers.

Storm-related sedimentation. The relative importance of sediment accumulation associated with storm-dominant period and storm duration is considered for different one-year-long periods, to avoid seasonal dependency (O18: October 2018 – October 2019, J19: January 2019-January 2020 and O19: October 2019 – October 2020, Extendend Data Fig. 2). It proves that storm surges account for more than 70% of the yearly sedimentation, although representing just 25% of the period duration on average. On the other hand, slight variation among different yearly periods confirms that this two-year-long dataset can explain the main seasonal variations of the processes.

Relation with geomorphological drivers. We report in Supplementary Table 1 the results of the cross-validation analysis performed to test the model validity. Model parameters are computed with a standard bootstrap resampling technique (Methods) and results are shown in Supplementary Table 2.

Supplementary Table 1. Cross-validation results. Error indicators of the 10-fold cross-validation (repeated 100 times) for the whole lagoon and for each study area (SF, SE and CO): Mean Absolute Errors (MAE), Mean Squared Error (MSE) and Root Mean Squared Error (RMSE). Train errors have subscript t and validation errors have subscript v.

Study area	MAEt ($g\ m^{-2}\ d^{-1}$)	MAEv ($g\ m^{-2}\ d^{-1}$)	MSEt $(g\ m^{-2}\ d^{-1})^2$	MSEv $(g\ m^{-2}\ d^{-1})^2$	RMSEt ($g\ m^{-2}\ d^{-1}$)	RMSEv ($g\ m^{-2}\ d^{-1}$)
Lagoon	8.71	9.40	199.68	235.76	14.11	13.54
SF	9.52	12.62	194.98	492.25	13.85	15.81
SE	3.92	8.22	40.66	401.81	6.30	11.37
CO	7.95	10.47	133.49	302.43	11.44	12.84

Supplementary Table 2. Sedimentation rate – tide relationship. Model parameter (SR = a*exp(b*MID)) for the whole lagoon and for each study area (SF, SE and CO). Standard errors are computed by a standard bootstrap technique.

Study area	a	b	R^2	MAE	p-value
Lagoon	1.95 ± 0.56	14.98 ± 1.16	0.71	8.63	<< 0.001
SF	3.39 ± 1.56	12.87 ± 2.10	0.68	9.96	<< 0.001
SE	0.09 ± 0.05	25.95 ± 2.12	0.96	3.92	<< 0.001
CO	3.40 ± 1.53	14.30 ± 2.56	0.64	7.64	<< 0.001

The effect of storm-surge barrier operation. To quantify the effect of operating the storm-surge barrier system on salt-marsh sedimentation, we computed the water levels under non-regulated and flood-regulated scenarios from October 2018 to January 2021 using the two-dimensional, finite-element *Wind-Wave-Tidal-Model* (WWTM)[1,2], which is based on a hydrodynamic module coupled with a wind-wave module.

The hydrodynamic module solves the 2D depth-integrated shallow water equations, suitably rewritten in order to reproduce wetting and drying processes in very shallow and irregular domains[3]:

$$\frac{\partial q_x}{\partial t} + \frac{\partial}{\partial x}\left(\frac{q_x^2}{Y}\right) + \frac{\partial}{\partial y}\left(\frac{q_x q_y}{Y}\right) - \left(\frac{\partial R_{xx}}{\partial x} + \frac{\partial R_{xy}}{\partial y}\right) + \frac{\tau_{tx}}{\rho} - \frac{\tau_{wx}}{\rho} + gY\left(\frac{\partial h}{\partial x}\right) = 0 \quad (1)$$

$$\frac{\partial q_y}{\partial t} + \frac{\partial}{\partial x}\left(\frac{q_x q_y}{Y}\right) + \frac{\partial}{\partial y}\left(\frac{q_y^2}{Y}\right) - \left(\frac{\partial R_{xy}}{\partial x} + \frac{\partial R_{yy}}{\partial y}\right) + \frac{\tau_{ty}}{\rho} - \frac{\tau_{wy}}{\rho} + gY\left(\frac{\partial h}{\partial y}\right) = 0 \quad (2)$$

$$\eta\left(\frac{\partial h}{\partial t}\right) + \frac{\partial q_x}{\partial x} + \frac{\partial q_y}{\partial y} = 0 \quad (3)$$

where t is time, the x, y subscripts represent the directions of a given variable in a Cartesian reference system, $\boldsymbol{q} = (q_x, q_y)$ is the flow rate per unit width, R_{ij} stands for the depth-averaged Reynolds stresses (i, j denoting either x or y coordinates), τ_{ti} and τ_{wi} are the bottom shear stress produced by tidal currents and wind-waves, respectively, ρ indicates the fluid density, g is the gravitational acceleration, Y denotes the water volume per unit area (i.e., the equivalent water depth), h is the free surface elevation, and η is the wet fraction of the computational domain which accounts for surface irregularities during the wetting and drying processes[3]. A semi-implicit staggered finite element method based on discontinuous Galerkin's approach is adopted to solve the governing equations[3].

The closure of the Reynolds stresses, which appear in the momentum equations along the two horizontal directions, is solved by introducing a suitable eddy viscosity, evaluated employing Smagorinsky's model[4]. The horizontal components of the Reynolds stresses then read:

$$R_{xx} = 2\nu_e\left(\frac{\partial q_x}{\partial x}\right) \quad (4)$$

$$R_{xy} = \nu_e\left(\frac{\partial q_x}{\partial y} + \frac{\partial q_y}{\partial x}\right) \quad (5)$$

The eddy viscosity ν_e differs from the standard one as it also encloses the contribution from the stresses generated by the subgrid momentum exchange, which is yet difficult to evaluate due to its dependence on the full three-dimensional morphology of the bottom surface[3]. The hydrodynamic module provides the wind-wave module with water levels and depth-averaged velocities that are used for calculating wave group celerity as well as for evaluating the influence of flow depth on wind-wave propagation.

The wind-wave module[1], based on the same computational grid of the hydrodynamic model, solves the wave action conservation equation[5]. The latter is simplified by assuming that the direction of

wave propagation instantaneously readjusts to match the wind direction (i.e., neglecting refraction). The wave action conservation equation describes the evolution of the wave action density (N_0) in the frequency domain and it reads[1]:

$$\frac{\partial N_0}{\partial t} + \frac{\partial}{\partial x} c'_{gx} N_0 + \frac{\partial}{\partial y} c'_{gy} N_0 = S_0 \quad (6)$$

where c'_{gx} and c'_{gy} represent the wave group celerity in the x and y direction respectively, and are used to approximate the propagation speed of N_0 [1,6], while S_0 represents all source terms describing the external phenomena contributing to wave energy variations, which can be either positive (wind energy input) or negative (bottom friction, whitecapping and depth-induced breaking). Based on the relationship between peak-wave period and local wind speed and water depth[7], the model is able to compute both the spatial and temporal distribution of the wave periods.

The WWTM model has been benchmarked against both hydrodynamic and wind-wave field data from the Venice lagoon (Italy)[1,2], Virginia Coast Reserve lagoons (USA)[8], and Cadiz bay (Spain)[9].

Once computed the water level time-series, MID is obtained, as for the measured water level, computing the mean of the water depth over the marsh when flooded. The site-specific exponential models (Figure 3) are then applied to compute sedimentation rate in the flood regulated and non-regulated scenarios.

In Extended Data Figure 3, we show the measured sediment accumulation (grey bars) together with the modelled ones in the non-regulated (teal bars) and flood-regulated scenario (yellow bars) for each period. Before October 2020 the barrier system was not active and sedimentation modelled in the non-regulated scenario well reproduces the measurements. In addition, our analyses show that measured deposition during periods of barrier activation are also well reproduced by the proposed regression, confirming that the exponential relationship is not only able to capture sediment accumulation dynamics under unimpeded conditions, but also their changes due to the closure of the flood barriers.

Accretion can be computed by combining sediment accumulation and bulk density (see Methods) and its changes through time in different scenarios are represented in Extended Data Figure 4, together with the cumulative accretion (continuous lines) and compared with kaolinite horizon marker measurements (black dots). During fair-weather periods, accretion under natural and flood-regulated conditions closely resemble each other, and sediment supply drop due to flood regulation during storm-dominated periods is sufficient to severely reduce the accretion in this scenario.

Sediment accumulation can be summed over yearly periods separately for the two scenarios to understand sedimentation changes due to flood-regulation at the annual time scale (Extended Data Figure 5 and Supplementary Tables 3 and 4). On average, flood-regulation would have reduced sedimentation by more than 25% in the period October 2018-October 2020 (30% and 26% for the first and the second monitored year, respectively).

Interestingly, all sites would have been affected by comparable absolute reductions (between 1235 and 1514 g m^{-2}), although the total sedimentation in the non-regulated scenario is rather different among study areas. The SE salt marsh is characterized by the lowest total yearly sedimentation (2554 g m^{-2} and 3183 g m^{-2} for O18 and O19, respectively) due to its position far from the main

channel network and facing a relatively sheltered tidal flat. Conversely, both the SF salt marsh, close to a major channel, and the CO salt marsh, exposed to the action of wind-waves propagating on a wide subtidal platform, display on average a sediment accumulation that is more than double than sediment accumulation in SE (6884 g m^{-2} in O18 and 7309 g m^{-2} in O19 for SF; 5741 g m^{-2} in O18 and 5024 g m^{-2} in O19 for CO). Consequently, sedimentation reduction due to flood-regulation will affect SE more severely than the other sites (-60% for O18 and -39% for O19 in SE; -21% for O18 and -20% for O19 in SF; -26% for O18 and -28% for O19 in CO – Extended Data Figure 5). Our results suggest that the relative amount of sedimentation reduction will diversely affect the different marshes and, hence, their specific capability to keep pace with sea-level rise.

Data collected in autumn 2020, i.e., October 2020-December 2020 when the barrier system was operational, provide a direct quantification of sedimentation reduction due to flood regulation, that can be compared with the sedimentation of the corresponding period of 2018 and 2019 (Extended Data Figure 6). Measurements are well-reproduced by modelled data both in non-regulated (grey and teal bar in autumn 2018 and 2019) and flood-regulated conditions (hatched grey and yellow bars in autumn 2020).

Supplementary Table 3. Sediment accumulation changes from October 2018 to October 2019 (O18). Sedimentation absolute change (3rd column) is computed as the difference between sedimentation in the regulated (2nd column) and non-regulated scenario (1st column). Sedimentation change as percentage is reported also in Supplementary Figure 6.

Year: O18 Case	Sedimentation non-regulated scenario ($g\ m^{-2}$)	Sedimentation regulated scenario ($g\ m^{-2}$)	Sedimentation absolute change ($g\ m^{-2}$)	Sedimentation change with respect to the non-regulated scenario as percentage (%)
SF_{O18}	6884.53	5411.03	-1473.50	-21 %
SE_{O18}	2554.84	1040.82	-1514.02	-60 %
CO_{O18}	5741.76	4240.01	-1501.75	-26 %
$mean_{O18}$	5060.38	3563.95	-1496.42	-30 %

Supplementary Table 4. Sediment accumulation changes from October 2019 to October 2020 (O19). Sedimentation absolute change (3rd column) is computed as the difference between sedimentation in the regulated (2nd column) and non-regulated scenario (1st column). Sedimentation change as percentage is reported also in Supplementary Figure 6.

Year: O19 Case	Sedimentation non-regulated scenario ($g\ m^{-2}$)	Sedimentation regulated scenario ($g\ m^{-2}$)	Sedimentation absolute change ($g\ m^{-2}$)	Sedimentation change with respect to the non-regulated scenario as percentage (%)
SF_{O19}	7309.86	5850.48	-1459.37	-20 %
SE_{O19}	3183.73	1948.57	-1235.16	-39 %
CO_{O19}	5024.30	3632.14	-1392.16	-28 %
$mean_{O19}$	5172.63	3810.40	-1362.23	-26 %

Sensitivity analysis of different activation thresholds. Mobile flood barriers can be operated at different activation thresholds, which might be increased by adopting complementary conventional or ecosystem-based measures[10]. In particular, for the Venice lagoon, the standard activation threshold is set at 110 cm above the local reference datum of Punta della Salute (ZPS) but the barriers can be activated also at lower levels to reduce flooding risk (up to 65 cm above ZPS, as it happened in October 2020). However, through additional local protection measures, the city might withstand higher water levels (reasonably up to 130 cm above ZPS). These changes in the activation thresholds would produce important differences in terms of marsh flooding and, hence, sedimentation, especially in the Venice lagoon where salt marshes occupy a relatively narrow range of elevations due to the microtidal regime[11,12].

We performed a sensitivity analysis to assess the effect of different activation thresholds on sedimentation (Supplementary Figure 3) using the methodology adopted in the present work. Different scenarios span from lower (i.e., 90 cm ZPS) to higher (i.e., 130 cm ZPS) activation thresholds, chosen in the reasonable activation range for the Venice lagoon. Lower activation thresholds dramatically reduce sediment accumulation on the marshes, up to 71% on average with the 90 cm ZPS activation threshold. Conversely, higher activation thresholds (i.e., 120 and 130 cm ZPS) only slightly affect sedimentation over the salt marshes.

In conclusion, although flood barriers negatively affect salt-marsh sedimentation, careful and integrated management can pave the way to a compromise between natural environment conservation and urban area protection.

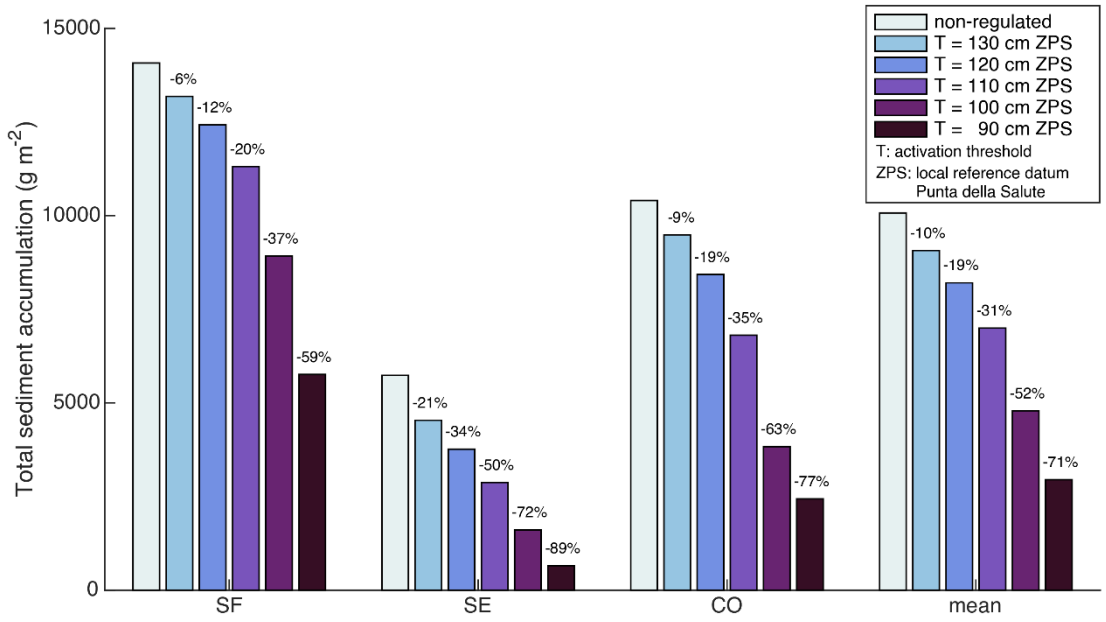

Supplementary Figure 3. Sensitivity analysis on different barrier activation thresholds. Comparison between total sediment accumulation for each study area and their mean over the whole period October 2018-October 2020 for the non-regulated scenario and different barrier activation thresholds (T). Percentage over bars indicate the reduction of each scenario with respect to the non-regulated one.

References

1. Carniello, L., D'Alpaos, A. & Defina, A. Modeling wind waves and tidal flows in shallow micro-tidal basins. Estuar. Coast. Shelf Sci. 92, 263–276 (2011).

2. Carniello, L., Defina, A., Fagherazzi, S. & D'Alpaos, L. A combined wind wave-tidal model for the Venice lagoon, Italy. J. Geophys. Res. Earth Surf. 110, 1–15 (2005).

3. Defina, A. Two-dimensional shallow flow equations for partially dry areas. Water Resour. Res. 36, 3251–3264 (2000).

4. Smagorinsky, J. General circulation experiments with the primitive equations: I. the basic experiment. Mon. Weather Rev. 91, 99–164 (1963).

5. Hasselmann, K. F. et al. Measurements of wind-wave growth and swell decay during the Joint North Sea Wave Project (JONSWAP). Ergaenzungsh. zur Dtsch. Hydrogr. Zeitschrift, R. A (1973).

6. Holthuijsen, L. H., Booij, N. & Herbers, T. H. C. A prediction model for stationary, short-crested waves in shallow water with ambient currents. Coast. Eng. 13, 23–54 (1989).

7. Young, I. R. & Verhagen, L. A. The growth of fetch limited waves in water of finite depth. Part 1. Total energy and peak frequency. Coast. Eng. (1996) doi:10.1016/S0378-3839(96)00006-3.

8. Mariotti, G. et al. Influence of storm surges and sea level on shallow tidal basin erosive processes. J. Geophys. Res. Ocean. (2010) doi:10.1029/2009JC005892.

9. Zarzuelo, C., López-Ruiz, A., D'Alpaos, A., Carniello, L. & Ortega-Sánchez, M. Assessing the morphodynamic response of human-altered tidal embayments. Geomorphology (2018) doi:10.1016/j.geomorph.2018.08.014.

10. Temmerman, S. et al. Ecosystem-based coastal defence in the face of global change. Nature 504, 79–83 (2013).

11. Goodwin, G. C. H. & Mudd, S. M. High platform elevations highlight the role of storms and spring tides in salt marsh evolution. Front. Environ. Sci. 7, 1–14 (2019).

12. D'Alpaos, A., Mudd, S. M. & Carniello, L. Dynamic response of marshes to perturbations in suspended sediment concentrations and rates of relative sea level rise. J. Geophys. Res. Earth Surf. 116, 1–13 (2011).